The Complex Organic Molecular Content in the L1498 Starless Core

Izaskun Jiménez-Serra[1] [iD], Anton I. Vasyunin[2] [iD], Silvia Spezzano[3], Paola Caselli[3] [iD], Giuliana Cosentino[4] [iD], and Serena Viti[5] [iD]

[1] Centro de Astrobiología (CSIC-INTA), Ctra. de Torrejón a Ajalvir km 4, E-28850, Torrejón de Ardoz, Spain; ijimenez@cab.inta-csic.es
[2] Ural Federal University, Kuybysheva st. 48, 620002, Ekaterinburg, Russian Federation, Russia
[3] Max Planck Institute for Extraterrestrial Physics, Giessenbachstrasse 1, D-85748, Garching, Germany
[4] Chalmers University of Technology, SE-41296, Gothenburg, Sweden
[5] University of Leiden, Niels Bohrweg 2, 2333 CA, Leiden, The Netherlands
Received 2021 February 16; revised 2021 May 13; accepted 2021 May 14; published 2021 August 13

Abstract

Observations carried out toward starless and prestellar cores have revealed that complex organic molecules are prevalent in these objects, but it is unclear what chemical processes are involved in their formation. Recently, it has been shown that complex organics are preferentially produced at an intermediate-density shell within the L1544 prestellar core at radial distances of ∼4000 au with respect to the core center. However, the spatial distribution of complex organics has only been inferred toward this core, and it remains unknown whether these species present a similar behavior in other cores. We report high-sensitivity observations carried out toward two positions in the L1498 starless core, the dust peak and a position located at a distance of ∼11,000 au from the center of the core where the emission of CH_3OH peaks. Similarly to L1544, our observations reveal that small O-bearing molecules and N-bearing species are enhanced by factors of ∼4–14 toward the outer shell of L1498. However, unlike L1544, large O-bearing organics such as CH_3CHO, CH_3OCH_3, or CH_3OCHO are not detected within our sensitivity limits. For N-bearing organics, these species are more abundant toward the outer shell of the L1498 starless core than toward the one in L1544. We propose that the differences observed between O-bearing and N-bearing species in L1498 and L1544 are due to the different physical structure of these cores, which in turn is a consequence of their evolutionary stage, with L1498 being younger than L1544.

Unified Astronomy Thesaurus concepts: Interstellar medium (847); Interstellar molecules (849); Astrochemistry (75); Molecular clouds (1072)

1. Introduction

Complex organic molecules (or COMs) are defined in astrochemistry as carbon-bearing compounds with at least six atoms in their structure (Herbst & van Dishoeck 2009). COMs were initially detected toward hot sources with temperatures ≥100 K such as massive hot cores (Hollis et al. 2000, 2006; Belloche et al. 2008, 2013) or low-mass warm cores (i.e., hot corinos; Bottinelli et al. 2004; Jorgensen et al. 2012). For this reason, it was first postulated that COMs only form on dust grains via hydrogenation and atom addition reactions (as for e.g., methanol; see Charnley et al. 1995; Watanabe & Kouchi 2002) or radical–radical reactions favored by the heating from the central protostar when the temperatures get higher than 30 K (see Garrod et al. 2008). This hypothesis implied that COMs could only form via hydrogenation in the coldest environments of the interstellar matter (ISM) such as dense dark cloud cores (with $T \leqslant 10$ K) and that, if formed, they would not be seen in the gas phase.

In the past decade, however, there has been a number of observational works that have changed our view of COM formation in the ISM. Large COM species, such as propylene (CH_2CHCH_3), acetaldehyde (CH_3CHO), dimethyl ether (CH_3OCH_3), or methyl formate (CH_3OCHO), have been found in the gas-phase toward dark cloud cores and starless/prestellar cores (Marcelino et al. 2007; Öberg et al. 2010; Bacmann et al. 2012; Cernicharo et al. 2012; Vastel et al. 2014; Jiménez-Serra et al. 2016; Soma et al. 2018; Agúndez et al. 2019; Yoshida et al. 2019; Scibelli & Shirley 2020). These observations have triggered a plethora of theoretical and experimental studies to understand COM formation at low temperatures

(see e.g., Rawlings et al. 2013; Vasyunin & Herbst 2013; Balucani et al. 2015; Ivlev et al. 2015; Ruaud et al. 2015; Chuang et al. 2016; Quénard et al. 2018; Shingledecker et al. 2018; Holdship et al. 2019; Jin & Garrod 2020), although no consensus has been reached yet.

To gain insight into the processes involved in the formation of COMs in cold sources, Jiménez-Serra et al. (2016) measured the abundance profiles of complex organics toward the L1544 prestellar core by means of high-sensitivity single-dish observations. Two positions in the core were observed: the dust peak of L1544 with a visual extinction $A_v \geqslant 60$ mag (the core's center) and the position where CH_3OH, the most abundant COM, peaks in L1544 (the methanol peak; Bizzocchi et al. 2014; Spezzano et al. 2016). The latter position is representative of an outer, lower-density shell located at a radius of 4000 au from the core's center and visual extinction $A_v \sim 15$–16 mag. The high-sensitivity observations not only revealed the presence of large COMs such as CH_3OCHO, CH_3OCH_3, and CH_2CHCN in L1544 (these species had remained elusive in previous campaigns; see Vastel et al. 2014) but also that they are factors of ∼2–10 more abundant toward the position of the methanol peak than toward L1544's center (Jiménez-Serra et al. 2016).

The modeling of the chemistry of O-bearing COMs in L1544 indeed predicts a peak in the radial abundance profiles of these species at a distance of ∼4000 au, coinciding with the location of the methanol peak and with the enhancement of O-bearing COMs (Vasyunin et al. 2017). The enhancement of these COMs in the lower-density shell of L1544 is driven by (Jiménez-Serra et al. 2016): (i) the freezing-out of CO onto dust grains, which triggers an active grain-surface chemistry; (ii) the intermediate visual

extinction at this shell (of $\sim$7–8 mag)[6], which is sufficient to prevent the UV photodissociation of COMs by the external interstellar radiation field; and (iii) the moderate H_2 gas number densities within the shell, which prevent the severe depletion of O-bearing COMs onto grains. All this suggests that O-bearing COMs are preferentially formed toward the low-density shells in starless/prestellar cores. For N-bearing COMs, the observations of Jiménez-Serra et al. (2016) show that the abundances of these species are also enhanced toward the position of the methanol peak in L1544 by small factors (of 1.2–1.8), although the peak intensity of their lines shows the opposite behavior to those of O-bearing COMs: while the O-bearing COM emission is stronger toward the position of the methanol peak, the N-bearing COM lines are brighter toward the core's center. Unlike those for O-bearing COMs, the formation mechanisms for N-bearing species in starless/prestellar cores remain vastly unexplored (see, e.g., Fedoseev et al. 2018).

Until recently, the spatial distribution of O-bearing and N-bearing species in starless and prestellar cores had been studied only toward a few of these cores (e.g., in L1544, L1498, and L1517B; Tafalla et al. 2006; Bizzocchi et al. 2014; Spezzano et al. 2017). However, Scibelli & Shirley (2020) have recently observed the emission from CH_3OH and CH_3CHO toward a large sample of starless and prestellar cores in the Taurus molecular cloud. Their results show that not only are these species prevalent across the sample (CH_3OH is detected in 100% of the sources, while CH_3CHO is detected in 70% of them) but also that the emission of CH_3OH is extended with morphologies similar to those found toward other cores such as L1544, L1498, or L1517B.[7] However, it remains unclear whether all starless/prestellar cores present the same level of chemical complexity regardless of their evolutionary stage or environment (see e.g., Lattanzi et al. 2020), or whether COMs and their precursors are distributed in all cores in a similar fashion to that observed in L1544.

The L1498 starless core belongs to the Taurus molecular complex, and it is located at a distance of 130 pc (Galli et al. 2019). By analyzing the kinematics of the high-density gas, Tafalla et al. (2004) found that the core is accreting material from the surrounding cloud as revealed by clear infall asymmetries in the CS line profiles. However, the N_2H^+ emission does not show any infall signatures, which implies that the core itself is not undergoing gravitational collapse. Compared to prestellar (grav- itationally-collapsing) cores such as L1544, L1498 shows a much flatter radial density distribution (Tafalla et al. 2004), and its deuterium fractionation (determined to be $N(N_2D^+)/N(N_2H^+)$) is only 4%, significantly lower than that found in L1544 ($\sim$23%– 25%; Crapsi et al. 2005; Redaelli et al. 2019). This lower deuterium fractionation is expected because it is the result of the lower CO depletion in L1498. Therefore, L1498 is likely at an earlier stage of evolution than L1544.

As L1544, L1498 also presents a methanol-rich shell. However, its methanol peak emission is located at distances farther away from the center of the core ($\sim$11,000 au in L1498 versus

$\sim$4000 au in L1544; Tafalla et al. 2006).[8] The visual extinction toward this position is also lower ($A_v \sim$ 7–8 mag; see below) than toward the methanol peak in L1544 ($A_v \sim$ 15–16 mag), which suggests that the behavior of O-bearing and N-bearing COMs, and of their precursors, may be different from that found in L1544.

In this paper, we present deep observations of O-bearing and N-bearing COMs toward two positions in the L1498 starless core. The goal is to not only establish the level of chemical complexity in this core, but also understand the formation mechanisms of COMs in cold cores as a function of evolution. The manuscript is organized as follows. Section 2 describes the observations, while Section 3 reports the results on the analysis of the COM and COM precursor emission for their excitation, column densities, and molecular abundances. Section 4 compares the abundances of the COMs and precursors measured toward L1498 with those obtained toward L1544. In Section 5, we model the chemistry of the observed COMs and precursors and compare the model predictions with the observations. Finally, in Section 6, we summarize our conclusions.

2. Observations

The observations of the L1498 starless core were carried out at 3 mm with the Instituto de Radioastronomía Milimétrica (IRAM) 30 m telescope (Granada, Spain) between 15–17 March 2017 and 20–22 May 2017 (project number 094-16). Two positions were observed toward the L1498 core (see Figure 1): the dust continuum peak, with coordinates α(J2000) = $04^h10^m53.70^s$, δ (J2000) = $25°10'18''.0$, and the position in the L1498 core where CH_3OH shows its peak emission, α(J2000) = $04^h10^m56.95^s$, δ (J2000) = $25°09'07''.9$. The latter position (hereafter the methanol peak) is indicated with a cross in Figure 1 (left panel), and it is located $\sim$83$''$ away (or $\sim$11,000 au at a distance of 130 pc) from L1498's dust peak (shown as a star in the same panel). Similarly to what is seen toward the L1544 prestellar core, L1498's methanol peak appears toward a high-density tail associated with the core (Figure 1). However, the ring-like methanol structure detected toward L1498 is more homogeneous than that observed toward L1544 (Figure 1 and Tafalla et al. 2006; Bizzocchi et al. 2014). Note, however, that the methanol peak in L1544 (Figure 1, right panel) is found at shorter radial distances ($\sim$4000 au) than those associated with the methanol peak in L1498 ($\sim$11,000 au; left panel of Figure 1).

The high-sensitivity 3 mm spectra were obtained in frequency-switching mode using a frequency throw of 7.14 MHz. The EMIR E090 receivers were tuned at 84.37 GHz, 94.82 GHz, and 110.16 GHz with rejections $\leqslant$10 dB. The observed frequency ranges are shown in Table 1. To avoid weak spurious features in the observed spectra, we carried out part of the observations by shifting slightly the central frequencies by $\pm$20 MHz (see also Jiménez-Serra et al. 2016). We used the narrow mode of the FTS spectrometer, which provided a spectral resolution of 50 kHz, equivalent to 0.15–0.18 km s^{-1} at 3 mm. Typical system temperatures ranged between 75 and 110 K and the telescope beam size was $\sim$24$''$–31$''$ between 79 and 101 GHz. The spectra were calibrated in units of antenna temperature, T_A^*, and converted into main beam temperature, T_{mb}, by using a beam efficiency of 0.81 at 79–101 GHz and of 0.78 at 102–111 GHz. The rms noise level ranged between $\sim$2 and 15 mK for the core's center position

---

[6] Note that the visual extinction toward the methanol peak is $A_v \sim$ 15–16 mag, but this is along the whole line of sight. The abundances in the models of Vasyunin et al. (2017) are calculated as a function of radius, and therefore, the visual extinction in the model has to be half that measured along the line of sight (i.e., $A_v \sim$ 7–8 mag; see Jiménez-Serra et al. 2016).
[7] Scibelli & Shirley (2020) mapped only seven cores from their sample in the Taurus molecular complex. Despite the poor angular resolution of their observations (beam of $\sim$1$'$), they find indications for chemical differentiation of CH_3OH toward all of the mapped cores.

---

[8] Note that the L1498 core morphology is elongated and the methanol shell presents radii between values r_{min} = 7800 au and r_{max} = 13,000 au.
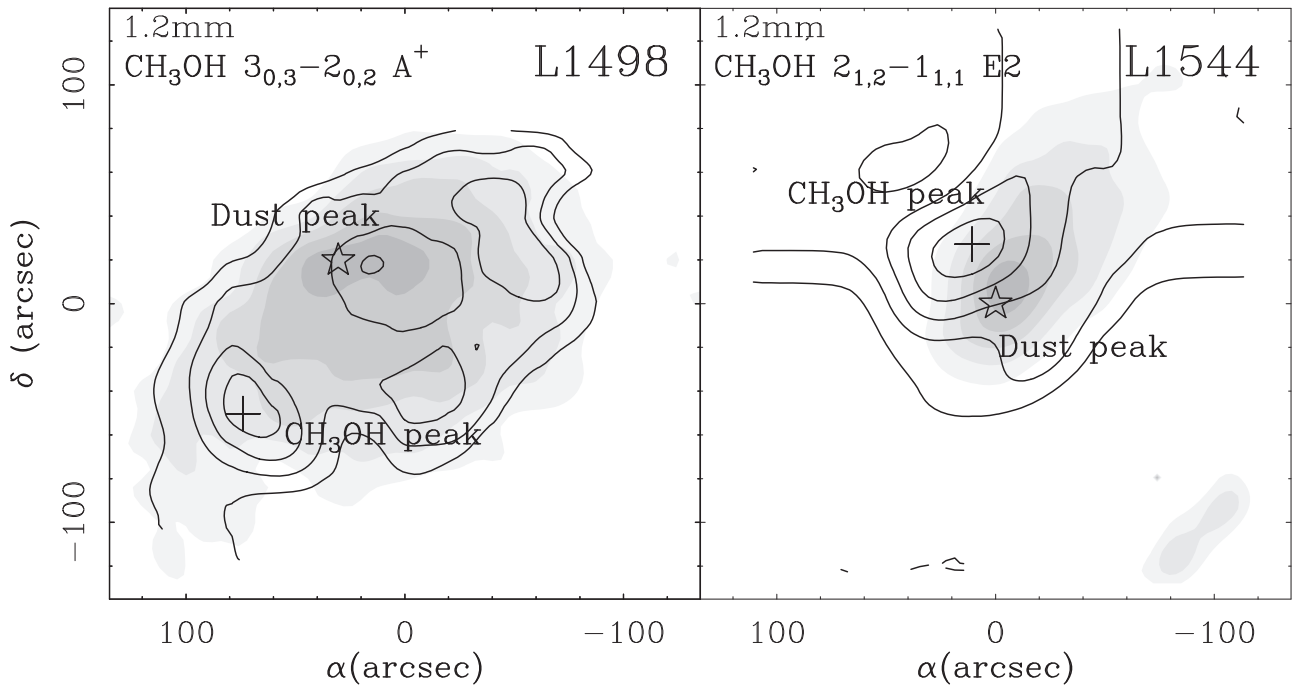
Figure 1. CH$_3$OH line integrated intensity maps (black contours) overlaid on the 1.2 mm dust continuum maps (grayscale) obtained toward the L1498 (left panel) and L1544 (right panel) cold cores (from Caselli et al. 2002; Tafalla et al. 2004, 2006; Spezzano et al. 2017). The grayscale indicates different percentage levels (15%, 30%, 45%, 60%, 75%, and 90%) with respect to the 1.2 mm dust continuum peak flux measured toward these cores (19.4 mJy/beam for L1498 and 224.8 mJy/beam for L1544). Contours correspond to the integrated intensity levels of 0.08, 0.12, 0.16, and 0.20 K km s^{-1} for the CH$_3$OH $3_{0,3} \rightarrow 2_{0,2}$ A$^+$ in L1498, and to levels of 0.11, 0.19, 0.27, 0.35, and 0.43 K km s^{-1} for the CH$_3$OH $2_{1,2} \rightarrow 1_{1,1}$ E2 in L1544. Stars indicate the location of the dust peaks in both cores while crosses show the coordinates of their methanol peaks. Note that the CH$_3$OH peak in L1544 is found at shorter radial distances ($\sim$4000 au) than those associated with the CH$_3$OH peak in L1498 ($\sim$11,000 au).

Table 1
Frequency Ranges, Velocity Resolution (δv), and rms Noise Level (rms) of Our Observations

Frequency (GHz)	δv (km s^{-1})	rms (mK)	
		Dust peak	CH$_3$OH peak
78.1–80.0	0.19	4.9	3.8
81.4–83.3	0.18	4.4	3.4
83.4–85.3	0.18	2.2	2.2
86.7–88.5	0.17	2.0	1.8
93.8–95.7	0.16	4.7	3.7
95.7–97.2	0.16	7.2	8.4
97.2–99.0	0.15	4.9	4.0
99.1–100.9	0.15	2.3	2.1
102.4–104.2	0.15	2.9	2.6
109.2–111.03	0.14	15.3	13.5

and between $\sim$1.8 and 14 mK for the methanol peak (see Table 1). The rms noise level for the frequencies between 95.7–97.2 and 109.2–111.03 was higher than that for the rest of the frequency ranges because they were sufficient to detect the observed CH$_3$OH and CH$_3$CN lines with high signal-to-noise ratios (S/Ns).

3. Results

3.1. COMs and COM Precursors Spectra

Table 2 presents the COMs and COM precursor molecules observed toward the dust and methanol peaks of L1498, along with their measured transitions, derived line parameters, and S/N in integrated intensity. The identification of the lines has been carried out using the Spectral Line Identification and Modelling (SLIM) tool within the MADCUBA package[9] (Martín et al. 2019). The spectroscopic entries are taken from the Cologne Database for Molecular Spectroscopy (Endres et al. 2016) and the Jet Propulsion Laboratory (JPL; Pickett et al. 1998).

Our observations have covered both O-bearing and N-bearing COMs and COM precursors. For O-bearing species, we have targeted methanol (CH$_3$OH), methoxy (CH$_3$O), CCCO, ketene (H$_2$CCO), formic acid (t-HCOOH), acetaldehyde (CH$_3$CHO), methyl formate (CH$_3$OCHO), dimethyl ether (CH$_3$OCH$_3$), cyclopropenone (c-C$_3$H$_2$O), and propynal (HCCCHO). As N-bearing COMs and precursors, we have cyanoacetylene (HC$_3$N), iso-cyanoacetylene (HCCNC), vinyl cyanide (CH$_2$CHCN), and methyl isocyanide (CH$_3$NC). A sample of their observed transitions is presented in Figures 2 and 3 for the dust and methanol peaks of the L1498 starless core, respectively.

Figures 2 and 3 show that species such as CH$_3$OH, CH$_3$O, CCCO, H$_2$CCO, HC$_3$N, HCCNC, and CH$_2$CHCN are detected either toward the dust or methanol peaks of the core or toward both positions. The detected lines lie above the 3σ level in integrated intensity, where 1σ is calculated as rms $\times \sqrt{\Delta v \times \delta v}$, with rms and δv being, respectively, the noise level and velocity resolution of the spectra (Table 1), and Δv the line width of the line. We are confident about the detection of the lines because they all show central radial velocities $\sim$7.8 km s^{-1}, the V_{LSR} of the source. In addition, except for CCCO, we have covered at least two

Table 2
COMs and COM Precursors Transitions Covered in Our L1498 Observations and Their Derived Line Parameters

Species	Line	Frequency	Dust peak				CH$_3$OH peak			
		(MHz)	Area[b] (mK km s^{-1})	Δv (km s^{-1})	V_{LSR} (km s^{-1})	S/N[c]	Area[b] (mK km s^{-1})	Δv (km s^{-1})	V_{LSR} (km s^{-1})	S/N[c]
CH$_3$OH	$2_{0,2} \to 1_{0,1}$ A	96741.371	140.0(1.5)[e]	0.228 (0.007)	7.796 (0.004)	93.3	160.0(1.8)[e]	0.224 (0.004)	7.754 (0.002)	88.9
	$2_{1,2} \to 1_{1,1}$ A	95914.310	$\leqslant$4.5	⋯	⋯	⋯	$\leqslant$5.4	⋯	⋯	⋯
	$2_{1,1} \to 1_{1,0}$ A	97582.798	$\leqslant$4.5	⋯	⋯	⋯	$\leqslant$5.4	⋯	⋯	⋯
	$2_{1,2} \to 1_{1,1}$ E	96739.358	101.6(1.5)	0.22(0.01)	7.805 (0.005)	23.4	116.3(1.8)	0.231 (0.014)	7.753 (0.006)	64.6
	$2_{0,2} \to 1_{0,1}$ E	96744.545	18.9(1.5)	0.22(0.01)	7.805 (0.005)	12.6	22.9(1.8)	0.231 (0.014)	7.753 (0.006)	12.7
	$2_{1,1} \to 1_{1,0}$ E	96755.501	$\leqslant$4.5	⋯	⋯	⋯	$\leqslant$5.4	⋯	⋯	⋯
CH$_3$O[a]	$F = 1 \to 0$, $\Lambda = -1$	82455.98	$\leqslant$3.6	⋯	⋯	⋯	$\leqslant$2.4	⋯	⋯	⋯
	$F = 2 \to 1$, $\Lambda = -1$	82458.25	4.3(1.2)[d]	0.42(0.13)	7.84(0.06)	3.6	$\leqslant$2.4	⋯	⋯	⋯
	$F = 2 \to 1$, $\Lambda = +1$	82471.82	4.3(1.2)	0.42(0.13)	7.84(0.06)	3.6	$\leqslant$2.4	⋯	⋯	⋯
	$F = 1 \to 0$, $\Lambda = +1$	82524.18	$\leqslant$3.6	⋯	⋯	⋯	$\leqslant$2.4	⋯	⋯	⋯
CCCO	$10 \to 9$	96214.619	4.7(1.4)	0.3(0.1)	7.82(0.06)	3.4	16.0(1.8)	0.43(0.08)	7.82(0.03)	8.9
t-HCOOH	$1_{1,1} \to 0_{0,0}$	87926.877	$\leqslant$1.5	⋯	⋯	⋯	$\leqslant$1.2	⋯	⋯	⋯
H$_2$CCO	$4_{1,3} \to 3_{1,2}$	81586.230	19.2(1.2)	0.37(0.03)	7.79(0.01)	16	29.3(0.8)	0.35(0.03)	7.769 (0.011)	36.6
	$5_{1,5} \to 4_{1,4}$	100094.514	14.3(0.6)	0.37(0.03)	7.79(0.01)	23.8	22.3(0.8)	0.35(0.03)	7.769 (0.011)	27.9
CH$_3$OCHO	$7_{2,6} \to 6_{2,5}$ A	84454.754	$\leqslant$1.8	⋯	⋯	⋯	$\leqslant$1.5	⋯	⋯	⋯
CH$_3$OCH$_3$	$3_{1,3} \to 2_{0,2}$ EE	82650.325	$\leqslant$3.6	⋯	⋯	⋯	$\leqslant$2.4	⋯	⋯	⋯
CH$_3$CHO	$5_{0,5} \to 4_{0,4}$ A	95963.465	$\leqslant$5.3	⋯	⋯	⋯	$\leqslant$5.4	⋯	⋯	⋯
c-C$_3$H$_2$O	$6_{1,6} \to 5_{1,5}$	79483.520	$\leqslant$4.2	⋯	⋯	⋯	$\leqslant$2.7	⋯	⋯	⋯
HCCCHO	$9_{0,9} \to 8_{0,8}$	83775.842	$\leqslant$1.8	⋯	⋯	⋯	$\leqslant$1.5	⋯	⋯	⋯
CH3CN	$6_0 \to 5_0$	110383.500	$\leqslant$9.7	⋯	⋯	⋯	25.7(3.1)	0.32(0.05)	7.72(0.02)	8.3
	$6_1 \to 5_1$	110381.372	$\leqslant$9.7	⋯	⋯	⋯	17.2(3.1)	0.32(0.05)	7.72(0.02)	5.5
	$6_2 \to 5_2$	110374.989	$\leqslant$9.7	⋯	⋯	⋯	$\leqslant$9.3	⋯	⋯	⋯
CH$_3$NC	$5_0 \to 4_0$	100526.541	$\leqslant$1.7	⋯	⋯	⋯	$\leqslant$1.2	⋯	⋯	⋯
CH$_2$CHCN	$9_{0,9} \to 8_{0,8}$	84946.000	6.3(0.6)	0.36(0.14)	7.78(0.06)	10.5	13.0(1.5)	0.34(0.08)	7.74(0.03)	8.7
	$9_{1,9} \to 8_{1,8}$	83207.505	4.4(1.2)	0.36(0.14)	7.78(0.06)	3.7	8.9(1.5)	0.34(0.08)	7.74(0.03)	5.9
	$9_{1,8} \to 8_{1,7}$	87312.812	3.8(0.5)	0.36(0.14)	7.78(0.06)	7.6	7.7(1.2)	0.34(0.08)	7.74(0.03)	6.4
	$10_{0,10} \to 9_{0,9}$	94276.636	$\leqslant$3.9	⋯	⋯	⋯	6.6(0.8)	0.34(0.08)	7.74(0.03)	8.3
	$10_{1,9} \to 9_{1,8}$	96982.442	$\leqslant$5.7	⋯	⋯	⋯	$\leqslant$5.4	⋯	⋯	⋯
HC$_3$N	$9 \to 8$	81881.468	856.7(1.2)	0.311 (0.009)	7.794 (0.003)	713.9	1102.2(0.8)	0.298 (0.002)	7.718 (0.001)	1377.8
	$11 \to 10$	100076.392	380.6(0.6)	0.311 (0.009)	7.794 (0.003)	634.3	514.9(0.8)	0.298 (0.002)	7.718 (0.001)	643.6
HCCNC	$8 \to 7$[d]	79484.131	33.9(1.4)	0.42(0.05)	7.81(0.02)	24.2	49.1(2.7)	0.36(0.06)	7.742 (0.024)	18.2
	$10 \to 9$[d]	99354.250	11.0(0.6)	0.42(0.05)	7.81(0.02)	18.3	17.7(0.4)	0.36(0.06)	7.742 (0.024)	44.3

Notes. Line profiles were fitted using MADCUBA (see Section 3.2).
[a] Hyperfine components of the $N = 1\text{-}0$, $K = 0$, $J = 3/2 \to 1/2$ transition of CH$_3$O.
[b] Upper limits are calculated as $3 \times$ rms $\times \sqrt{\Delta v \times \delta v}$, with rms the noise level, Δv the line width, and δv the velocity resolution of the spectrum.
[c] This refers to the S/N in the integrated intensity area.
[d] Hyperfine structure not resolved.
[e] Errors in the line area are calculated as rms $\times \sqrt{\Delta v \times \delta v}$.
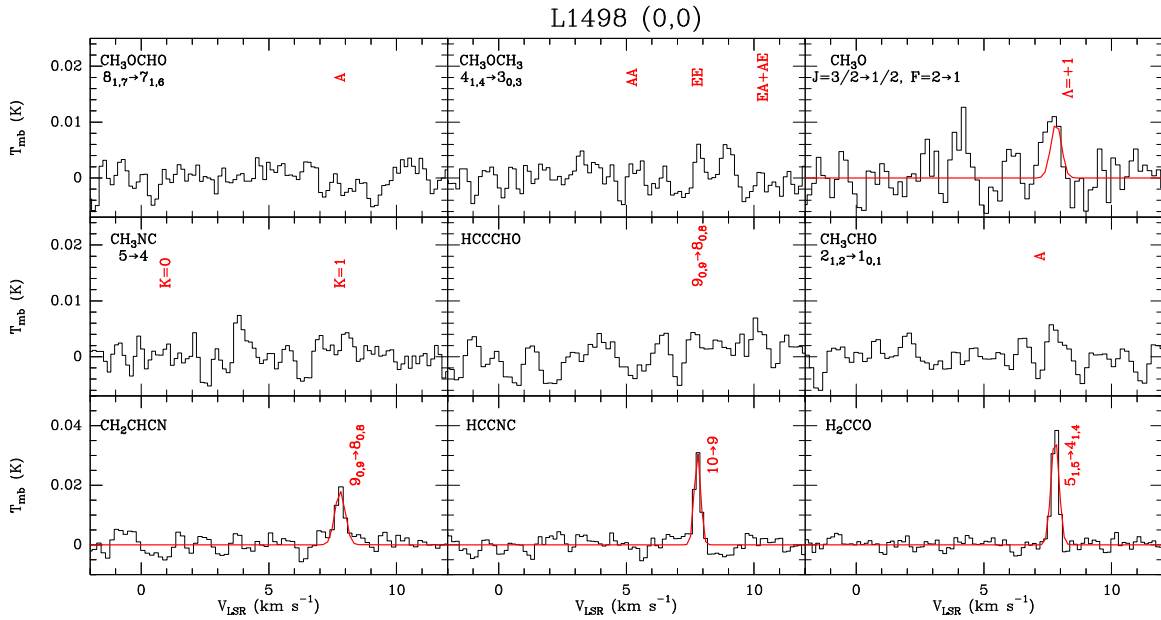
Figure 2. Sample of COM lines observed toward L1498's dust continuum peak. Red lines show the Gaussian line fits derived for the COMs and COM precursor transitions.
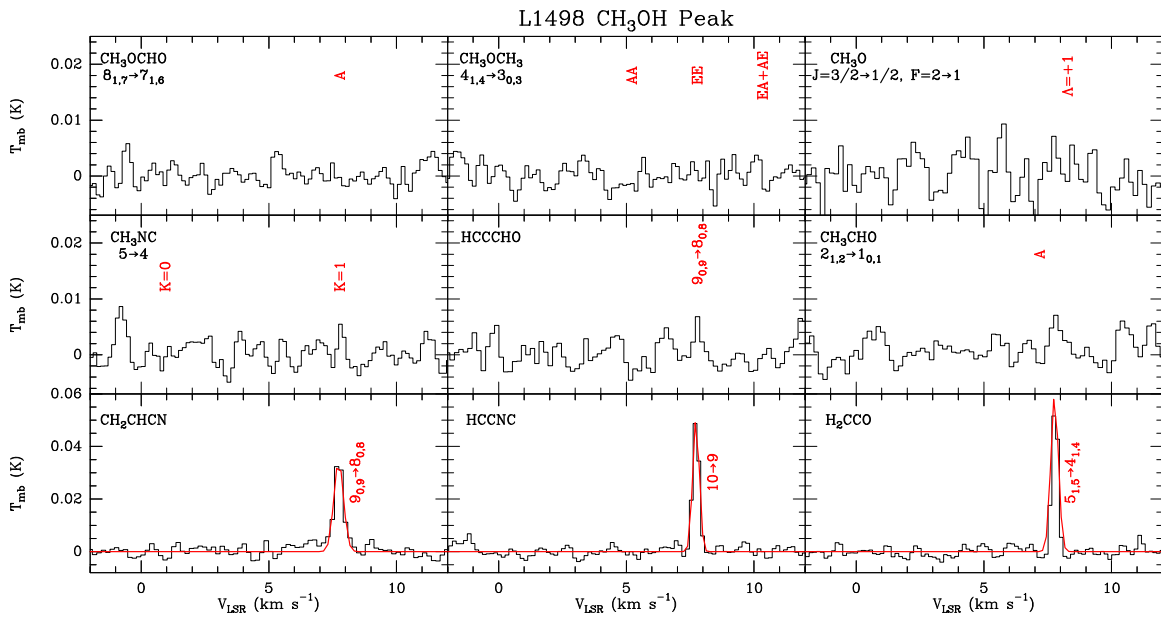

Figure 3. Sample of COM lines observed toward the position of the methanol peak in L1498. Red lines show the Gaussian line fits derived for the COMs and COM precursor transitions.

transitions for each detected species, which is enough for the correct identification of the molecular species because the level of line blending in starless/prestellar cores is expected to be low (line widths of $\sim$0.3–0.4 km s^{-1}; see Table 2).

From Figures 2 to 3, and from Table 2, we find that the emission of the detected COMs and precursors tends to be brighter toward the position of the methanol peak with respect to the core's center except for CH$_3$O, which is only detected toward L1498's dust peak. Note, however, that the detected lines of CH$_3$O are weak (S/N = 3.6; Table 2). For the rest of the molecules (t-HCOOH, CH$_3$CHO, CH$_3$OCHO, CH$_3$OCH$_3$, c-C$_3$H$_2$O, HCCCHO, and CH$_3$NC), we have not detected any feature. The upper limits have been obtained from those

transitions expected to be the brightest at the $T_{\rm ex}$ of the COM emission in the L1498 core (Section 3.2).

3.2. Excitation Analysis of COMs and COM Precursors

Except for CH$_3$OH (see below), the excitation temperature, $T_{\rm ex}$, of the COM species with at least two transitions covered in our observations (i.e., H$_2$CCO, CH$_2$CHCN, HC$_3$N, and HCCNC; see Table 2) has been determined using the SLIM package within MADCUBA. For CH$_3$O, the AUTOFIT tool did not converge because the targeted lines have similar upper-level energies and therefore, the $T_{\rm ex}$ was fixed to that obtained for H$_2$CCO, another COM precursor ($T_{\rm ex} = 5.8 \pm 0.8$ K;

Table 3
Excitation Temperatures, Column Densities, and Abundances of COMs and COM Precursors toward the Dust and Methanol Peaks in L1498

Molecule	Dust Peak			Methanol Peak		
	T_{ex}	N_{obs} (cm^{-2})	χ_{obs}[a]	T_{ex}	N_{obs} (cm^{-2})	χ_{obs}[a]
CH$_3$OH-A	10[d]	3.1×10^{12}[d]	8.9×10^{-11}[d]	10[d]	4.7×10^{12}[d]	6.5×10^{-10}[d]
CH$_3$OH-E	10[d]	3.4×10^{12}[d]	9.7×10^{-11}[d]	10[d]	4.0×10^{12}[d]	5.6×10^{-10}[d]
CH$_3$OH (Total)	⋯	6.5×10^{12}[d]	1.9×10^{-10}[d]	⋯	8.7×10^{12}[d]	1.2×10^{-9}[d]
CH$_3$O	5.8[b]	$(1.2 \pm 0.4) \times 10^{11}$	$(3.6 \pm 1.2) \times 10^{-12}$	6.0[b]	$\leqslant 1.2 \times 10^{11}$	$\leqslant 1.7 \times 10^{-11}$
CCCO	5.8[b]	$(3.9 \pm 1.5) \times 10^{11}$	$(1.2 \pm 0.5) \times 10^{-11}$	6.0[b]	$(1.2 \pm 0.2) \times 10^{12}$	$(1.7 \pm 0.3) \times 10^{-10}$
t-HCOOH	5.8[b]	$\leqslant 4.6 \times 10^{12}$	$\leqslant 1.4 \times 10^{-10}$	6.0[b]	$\leqslant 6.6 \times 10^{12}$	$\leqslant 9.2 \times 10^{-10}$
H$_2$CCO	5.8 ± 0.8[c]	$(2.6 \pm 0.6) \times 10^{12}$	$(7.8 \pm 1.8) \times 10^{-11}$	6.0 ± 0.3[c]	$(4.5 \pm 0.2) \times 10^{12}$	$(6.2 \pm 0.3) \times 10^{-10}$
CH$_3$OCHO	5.8[b]	$\leqslant 1.3 \times 10^{12}$	$\leqslant 3.9 \times 10^{-11}$	6.0[b]	$\leqslant 1.1 \times 10^{12}$	$\leqslant 1.5 \times 10^{-10}$
CH$_3$OCH$_3$	5.8[b]	$\leqslant 3.9 \times 10^{11}$	$\leqslant 1.2 \times 10^{-11}$	6.0[b]	$\leqslant 4.4 \times 10^{11}$	$\leqslant 6.1 \times 10^{-11}$
CH$_3$CHO	5.8[b]	$\leqslant 3.0 \times 10^{11}$	$\leqslant 9.0 \times 10^{-12}$	6.0[b]	$\leqslant 1.4 \times 10^{11}$	$\leqslant 1.9 \times 10^{-11}$
c-C$_3$H$_2$O	5.8[b]	$\leqslant 3.9 \times 10^{10}$	$\leqslant 1.2 \times 10^{-12}$	6.0[b]	$\leqslant 2.9 \times 10^{10}$	$\leqslant 4.0 \times 10^{-12}$
HCCCHO	5.8[b]	$\leqslant 2.0 \times 10^{11}$	$\leqslant 6.0 \times 10^{-12}$	6.0[b]	$\leqslant 2.0 \times 10^{11}$	$\leqslant 2.8 \times 10^{-11}$
CH$_3$CN	5.6[b]	$\leqslant 8.3 \times 10^{10}$	$\leqslant 2.4 \times 10^{-12}$	15.9 ± 5.8	$(1.0 \pm 0.1) \times 10^{11}$	$(1.4 \pm 0.1) \times 10^{-11}$
CH$_3$NC	5.6[b]	$\leqslant 1.0 \times 10^{10}$	$\leqslant 3.0 \times 10^{-13}$	6.0[b]	$\leqslant 7.8 \times 10^{9}$	$\leqslant 1.1 \times 10^{-12}$
CH$_2$CHCN	4.1 ± 0.3[c]	$(1.3 \pm 0.4) \times 10^{12}$	$(3.9 \pm 1.2) \times 10^{-11}$	4.9 ± 0.3[c]	$(1.1 \pm 0.2) \times 10^{12}$	$(1.5 \pm 0.3) \times 10^{-10}$
HC$_3$N	6.4 ± 0.3[c]	$(1.6 \pm 0.3) \times 10^{13}$	$(4.8 \pm 0.9) \times 10^{-10}$	6.5 ± 0.7[c]	$(2.2 \pm 1.0) \times 10^{13}$	$(3.1 \pm 1.4) \times 10^{-9}$
HCCNC	5.6 ± 0.9[c]	$(7.8 \pm 4.0) \times 10^{11}$	$(2.4 \pm 1.2) \times 10^{-11}$	6.0 ± 1.3[c]	$(9.4 \pm 5.7) \times 10^{11}$	$(1.3 \pm 0.8) \times 10^{-10}$

Notes.
[a] Molecular abundances calculated using a H$_2$ column density of 3.5×10^{22} cm^{-2} for the dust continuum peak and of 7.2×10^{21} cm^{-2} for the position of the methanol peak (see Section 3.3 for details).
[b] Fitting solutions could only be obtained by fixing T_{ex} within the MADCUBA-SLIM tool (Martín et al. 2019).
[c] Errors correspond to 1σ uncertainties in MADCUBA.
[d] The CH$_3$OH column densities have been calculated using RADEX (Van der Tak et al. 2007). The value under T_{ex} refers to the assumed kinetic temperature T_{kin} in the RADEX calculations.

Table 3). The same was done for CCCO, for which only one transition is available in our data set. The T_{ex} derived from the COM emission lie between 4.1 and 6.4 K for the dust peak, and between 4.9 and 6.5 K toward the methanol peak. These T_{ex} are similar to those measured toward other starless/prestellar cores (see Bizzocchi et al. 2014; Vastel et al. 2014; Jiménez-Serra et al. 2016; Punanova et al. 2018; Harju et al. 2020; Scibelli & Shirley 2020), and suggest subthermal excitation of the COM emission in the L1498 core given that the kinetic temperature of the gas is $\sim$10 K within the inner $\sim$80″ (or 11,000 au; Tafalla et al. 2004).

The column densities of these COMs and COM precursors toward both the dust and methanol peaks in L1498 are reported in Table 3. The upper limits to the column densities of the molecular species not detected (e.g., CH$_3$OCHO or CH$_3$OCH$_3$) were calculated assuming $T_{ex} = 5.8$ K and 6.0 K for the dust and methanol peaks, respectively, and are also reported in this table.

For CH$_3$OH (A and E species), we used RADEX instead of MADCUBA (Van der Tak et al. 2007) because MADCUBA performs the fitting of the molecular lines using the LTE approximation. We assume a kinetic temperature of $T_{kin} = 10$ K (Tafalla et al. 2004). The fit of the CH$_3$OH lines was achieved considering a H$_2$ gas density of $\sim 4 \times 10^4$ cm^{-3} (consistent with the one expected from the H$_2$ radial gas density profile derived by Tafalla et al. (2004) at a distance of $\sim$83″; see Section 5) and assuming column densities of 3.1×10^{12} cm^{-2}/3.4×10^{12} cm^{-2} for the A/E species toward L1498's dust peak and of 4.7×10^{12} cm^{-2}/4.0×10^{12} cm^{-2} for the A/E species toward the methanol peak. The CH$_3$OH A/E abundance ratios are $\sim$0.9 and $\sim$1.2 toward the dust and methanol peaks, respectively. These values are similar to those derived toward L1544 and other molecular dark clouds such as L183, TMC-1, or B335 (Friberg et al. 1988; Bizzocchi et al. 2014) and fall between the expected

high temperature value of $\sim$1.0 and the one at 10 K ($\sim$0.7; see Wirström et al. 2011).

3.3. COM Abundance Profiles in L1498

To calculate the abundances of the observed COMs and precursors, we need to determine the H$_2$ column density toward the dust and methanol peaks of L1498. For the core center, we use the H$_2$ column density of $\sim 3.5 \times 10^{22}$ cm^{-2} inferred by Tafalla et al. (2004) from MAMBO 1.2 mm data. The H$_2$ gas density profile of the L1498 starless core is flat within the inner 30″, which engulfs the radius associated with half the beam of the IRAM 30 m observations at 3 mm (radius of $\sim$13″). For the position of the methanol peak, we use the H$_2$ column density map of the Taurus molecular cloud obtained by Spezzano et al. (2016) from Herschel data at 250, 350, and 500 μm assuming a dust optical depth index of $\beta = 1.5$. The H$_2$ column density toward L1498's methanol peak (i.e., at a distance of $\sim$83″ with respect to the core's center) is 7.2×10^{21} cm^{-2}. While the H$_2$ column density of $\sim 3.5 \times 10^{22}$ cm^{-2} toward the dust peak corresponds to a visual extinction of $A_v \sim 37$ mag, the H$_2$ column density of 7.2×10^{21} cm^{-2} measured toward the methanol peak corresponds to a visual extinction of $A_v \sim 7.7$ mag using the Bohlin et al. (1978) formula (or N(H$_2$)/$A_v = 0.94 \times 10^{21}$ cm^{-2}).

Table 3 reports the derived abundances of the COMs and COM precursors shown in Table 2. Table 3 reveals a general trend for these species to be enhanced toward the position of the methanol peak of L1498. The O-bearing species present the largest enhancements with CCCO and H$_2$CCO being, respectively, factors of $\sim$14 and $\sim$8 more abundant toward the methanol peak than toward the core center. For the N-bearing molecules, their abundances are enhanced by factors of $\sim$4–6 toward the outer part of the L1498 starless core. This COM enhancement is similar to that reported toward the L1544

Table 4

Excitation Temperatures, Column Densities, and Abundances of CH$_3$OH, CCCO, H$_2$CCO, t-HCOOH, CH$_3$CN, and HC$_3$N toward the Dust and Methanol Peaks in L1544

Molecule	Dust Peak			Methanol Peak		
	T_{ex}	N_{obs} (cm^{-2})	χ_{obs}[a]	T_{ex}	N_{obs} (cm^{-2})	χ_{obs}[a]
CH$_3$OH-A	⋯	0.7×10^{13}[d]	0.2×10^{-9}[d]	⋯	2.4×10^{13}[d]	4×10^{-9}[d]
CH$_3$OH-E	⋯	0.7×10^{13}[d]	0.2×10^{-9}[d]	⋯	2.4×10^{13}[d]	4×10^{-9}[d]
CH$_3$OH (Total)	⋯	1.4×10^{13}[d]	0.4×10^{-9}[d]	⋯	4.8×10^{13}[d]	8×10^{-9}[d]
CCCO	5.6 ± 1.3[c]	$(8.9 \pm 1.2) \times 10^{11}$[e]	$(1.7 \pm 0.2) \times 10^{-11}$	5.9[b]	$(7.2 \pm 1.3) \times 10^{11}$[e]	$(4.8 \pm 0.9) \times 10^{-11}$
t-HCOOH	12.6 ± 6.9[c]	$(4.8 \pm 0.9) \times 10^{11}$[e]	$(8.9 \pm 1.7) \times 10^{-12}$	5.9[b]	$(4.0 \pm 1.2) \times 10^{10}$[e]	$(2.7 \pm 0.8) \times 10^{-12}$
H$_2$CCO	4.9 ± 0.2[f]	$(1.5 \pm 0.2) \times 10^{13}$[f]	$(2.8 \pm 0.4) \times 10^{-10}$	5.9 ± 0.8[c]	$(9.8 \pm 2.3) \times 10^{12}$[e]	$(6.5 \pm 1.5) \times 10^{-10}$
CH$_3$CN	8.7 ± 1.3[c]	$(1.5 \pm 0.2) \times 10^{11}$[e]	$(2.8 \pm 0.4) \times 10^{-12}$	5.9[b]	$\leqslant 9.1 \times 10^{10}$[e]	$\leqslant 6.1 \times 10^{-12}$
HC$_3$N	5.5 ± 0.2[c]	$(1.0 \pm 0.3) \times 10^{14}$[e]	$(1.9 \pm 0.6) \times 10^{-9}$	4.8[b]	$(4.2 \pm 0.4) \times 10^{13}$[e]	$(2.8 \pm 0.3) \times 10^{-9}$

Notes.

[a] Molecular abundances calculated using an H$_2$ column density of 5.4×10^{22} cm^{-2} for the dust continuum peak and of 1.5×10^{22} cm^{-2} for the position of the methanol peak (Jiménez-Serra et al. 2016).

[b] Fitting solutions could only be obtained by fixing T_{ex} within the MADCUBA-SLIM analysis tool (Martín et al. 2019).

[c] Errors correspond to 1σ uncertainties in MADCUBA.

[d] Taken from the non-LTE analysis carried out by Punanova et al. (2018).

[e] Obtained using the data from Jiménez-Serra et al. (2016).

[f] Note that this molecule was also observed by Vastel et al. (2014) but they obtained a $T_{ex} = 27 \pm 1$ K. We thus use the data from Jiménez-Serra et al. (2016), which give a closer T_{ex} to the ones inferred for the other species.

prestellar core (Jiménez-Serra et al. 2016). In Section 4, we compare the COM and COM precursor abundance profiles measured toward these two cores, L1498 and L1544.

We note that the H$_2$ column density derived for the position of the dust peak of L1498 but using Herschel data is $\sim 10^{22}$ cm^{-2}, a factor of ~ 4 lower than that measured by MAMBO at 1.2 mm. This is due to the fact that Herschel underestimates the total amount of dust present toward this region because it preferentially probes the dust grain population from the outer layers of the core (Chacón-Tanarro et al. 2019). In addition, the large Herschel beam can dilute possible centrally concentrated structures, such as toward the center of L1544. This is the reason why we use the millimeter data to measure the total H$_2$ column density toward the innermost regions of L1498.

For the position of the methanol peak, the H$_2$ column density measured using Herschel and MAMBO data is similar. Indeed, the H$_2$ column density obtained from the MAMBO 1.2 mm map (M. Tafalla, private communication) is $\sim 1.3 \times 10^{22}$ cm^{-2}, i.e., only a factor of ~ 1.8 higher than that derived using Herschel (7.2×10^{21} cm^{-2}; see above). This factor is smaller than the COMs abundance enhancements measured in L1498's methanol peak with respect to the core center (~ 4–14), which implies that the observed increase in the abundance of COMs toward the outer regions of L1498 is real. We opt for the use of the Herschel-based H$_2$ column density toward L1498's methanol peak, because (i) the calculation of and comparison with the COMs abundances toward L1544 is done in the same manner (see Jiménez-Serra et al. 2016); (ii) the Herschel beam of $\sim 35''$ is closer to the one of the IRAM 30 m observations ($\sim 30''$ versus $\sim 11''$ of the MAMBO observations); and (iii) the MAMBO observations toward the outer parts of the core may be affected by the large-scale filtering produced by the chopping technique used in ground-based telescopes.

4. Comparison with L1544

Vastel et al. (2014) reported the abundances of the COMs and precursor species CH$_3$OH, CCCO, H$_2$CCO, and t-HCOOH toward the dust peak of the L1544 prestellar core. In

Jiménez-Serra et al. (2016), two different positions in this core were observed but no abundances were provided for the latter COM precursor species. Therefore, in this section, we take the abundances of CH$_3$OH (A and E species) from Punanova et al. (2018, who obtained a radial profile of the abundance of CH$_3$OH) and calculate the abundances of CCCO, H$_2$CCO, and t-HCOOH toward both the dust and methanol peaks of L1544 using the IRAM 30 m data from Jiménez-Serra et al. (2016; please refer to this article for the details of the observations). In this way, we can compare these results with those obtained toward the L1498 starless core. In our analysis, we also include the N-bearing molecules HC$_3$N and CH$_3$CN.

Table 4 collects the excitation temperatures (T_{ex}), column densities (N_{obs}), and molecular abundances of all these molecules measured toward the dust and methanol peaks of L1544. Note that the column densities derived for these species toward the dust peak of L1544 are very similar to those calculated independently by Lattanzi et al. (2020) for the same position within this core.

In Figure 4, we present the comparison of the abundances of COMs and COM precursors measured toward the dust peaks and methanol peaks of the cold cores L1544 (yellow and red, respectively) and L1498 (cyan and dark blue, respectively). As mentioned in Section 3.3, all of the detected COMs and COM precursors, except t-HCOOH in L1544, are enhanced toward the position of the methanol peaks in both L1498 and L1544. However, the abundances of O-bearing and N-bearing species are significantly different in L1498 with respect to L1544. While large O-bearing COMs such as CH$_3$CHO, CH$_3$OCHO, or CH$_3$OCH$_3$ are clearly detected in L1544, we only report upper limits to the abundance of these molecules in L1498. Especially clear is the case of CH$_3$CHO, which is relatively abundant in L1544 (with an abundance of $\sim 2 \times 10^{-10}$ toward the methanol peak; Figure 4), but it is not detected in L1498. Interestingly, the COM precursor CH$_3$O shows an opposite behavior toward both cores: while CH$_3$O is clearly enhanced toward the methanol peak of L1544, this molecule is only detected toward the core center of L1498. However, note that
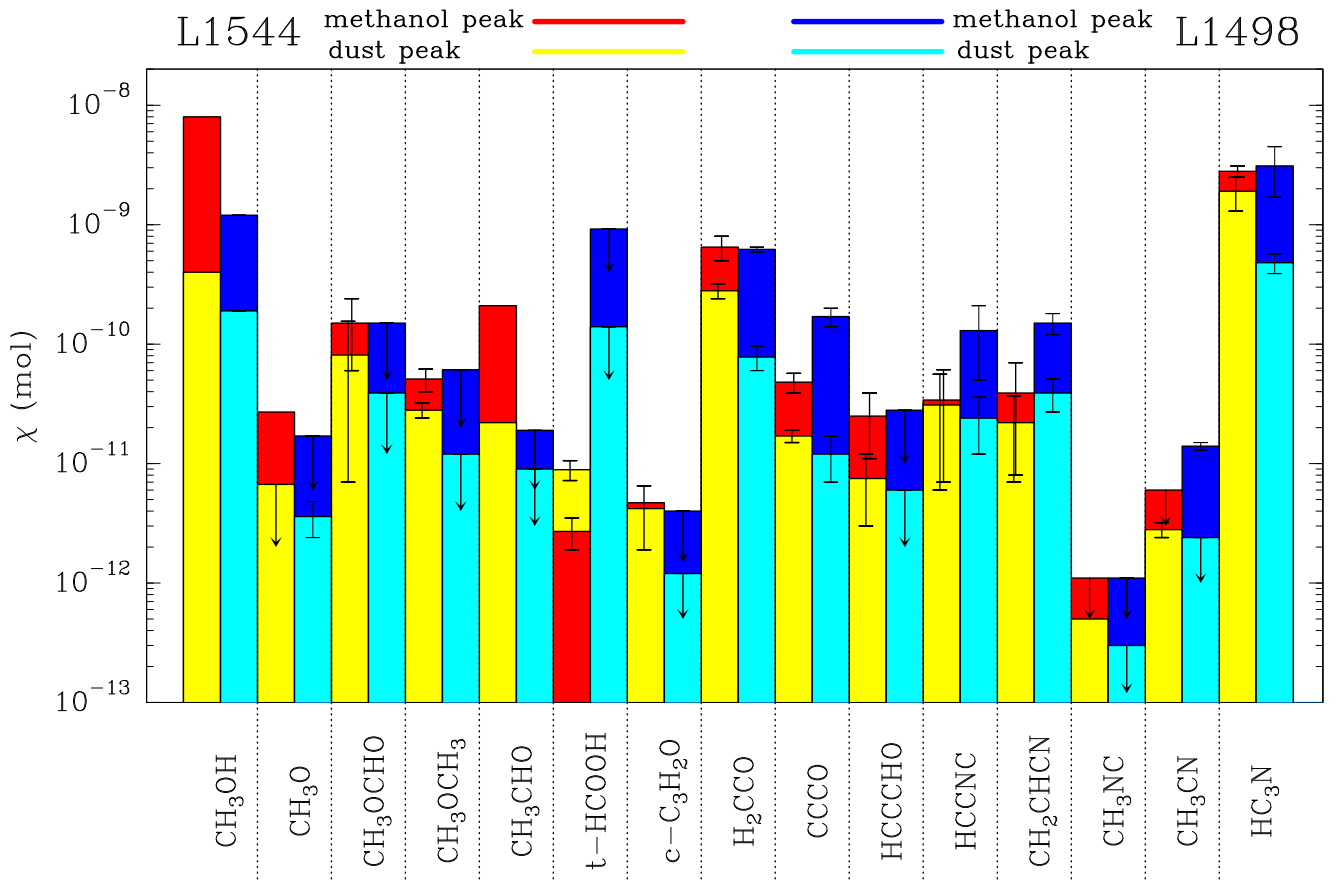
Figure 4. Histogram comparing the abundances of COMs and COM precursors measured toward the methanol and dust peaks in L1498 and L1544. Molecules are labeled at the bottom. Error bars correspond to 1σ uncertainties in the column densities calculated by MADCUBA, and arrows indicate upper limits. The color legend is as follows: red—methanol peak in L1544; yellow—dust peak in L1544; dark blue—methanol peak in L1498; and cyan—dust peak in L1498. The abundances of the COMs and COM precursors have either been extracted from Jiménez-Serra et al. (2016) and Punanova et al. (2018) or have been calculated from the data used in Jiménez-Serra et al. (2016).

Table 5
Measured and Modeled Abundances of Complex Organic Molecules in L1498

Species	Dust Peak			Methanol Peak		
	$N(X)/N(H_2)_{obs}$	$N(X)/N(H_2)_{mod}$	Agreement	$N(X)/N(H_2)_{obs}$	$N(X)/N(H_2)_{mod}$	Agreement
CH_3OH	1.9×10^{-10}	7.7×10^{-9}	−	1.2×10^{-9}	8.6×10^{-9}	+
CH_3O	3.6×10^{-12}	7.5×10^{-12}	+	$\leqslant 1.7 \times 10^{-11}$	7.3×10^{-13}	+
C_3O	1.2×10^{-11}	1.1×10^{-10}	+	1.7×10^{-10}	1.6×10^{-10}	+
$HCOOH$	$\leqslant 1.4 \times 10^{-10}$	7.2×10^{-10}	+	$\leqslant 9.2 \times 10^{-10}$	2.7×10^{-10}	+
H_2CCO	7.8×10^{-11}	8.0×10^{-10}	−	6.2×10^{-10}	4.6×10^{-10}	+
$HCOOCH_3$	$\leqslant 3.9 \times 10^{-11}$	4.4×10^{-13}	+	$\leqslant 1.5 \times 10^{-10}$	8.3×10^{-14}	+
CH_3OCH_3	$\leqslant 1.2 \times 10^{-11}$	1.4×10^{-13}	+	$\leqslant 6.1 \times 10^{-11}$	4.7×10^{-14}	+
CH_3CHO	$\leqslant 9.0 \times 10^{-12}$	2.1×10^{-11}	+	$\leqslant 1.9 \times 10^{-11}$	1.2×10^{-11}	+
$HCCCHO$	$\leqslant 7.2 \times 10^{-12}$	8.0×10^{-13}	+	$\leqslant 3.2 \times 10^{-11}$	4.6×10^{-13}	+
CH_3CN	$\leqslant 2.4 \times 10^{-12}$	8.7×10^{-13}	+	1.4×10^{-11}	3.0×10^{-12}	+
CH_3NC	$\leqslant 3.0 \times 10^{-13}$	8.7×10^{-13}	+	$\leqslant 1.1 \times 10^{-12}$	3.2×10^{-12}	+
CH_2CHCN	3.9×10^{-11}	1.6×10^{-13}	−	$1.5e \times 10^{-10}$	1.3×10^{-13}	−
HC_3N	5.0×10^{-10}	1.7×10^{-10}	+	3.2×10^{-9}	3.5×10^{-10}	+

the upper limit to the abundance of CH_3O toward L1498's methanol peak is still consistent with a possible enhancement of this species in the outer shells of the core.

For the N-bearing COMs and precursors, Figure 4 shows that these species not only are in general more abundant toward L1498 than in L1544, but they also present larger enhancements toward L1498's methanol peak than toward the one in

L1544 (the enhancements are by factors 4–6 in L1498 versus factors 1.2–1.8 in L1544; see Section 3.3 and Jiménez-Serra et al. 2016). As discussed in Section 5, the observed differences in the abundance profiles of O-bearing and N-bearing species in L1498 and L1544 are due to the different physical structure of the cores, which in turn is likely associated with their evolutionary stage.
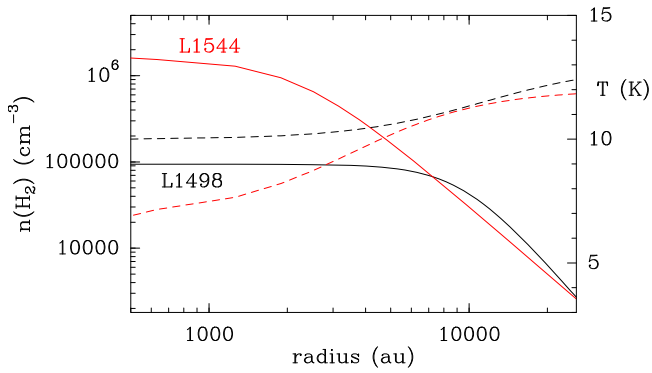
Figure 5. Radial distribution of the H$_2$ volume gas density (solid lines) and temperature (dashed lines) assumed for the L1498 starless core as a function of radius (in black; see also Section 5 and Tafalla et al. 2004). For comparison, we also show the physical structure of the L1544 prestellar core determined by Chacón-Tanarro et al. (2019, in red).

5. Modeling the Formation of COMs in L1498

To understand the observed abundances of O-bearing and N-bearing COMs in L1498 and their differences with respect to L1544, we have modeled the chemistry of COMs using the 1D approach previously used in Vasyunin et al. (2017) but applied to the case of L1498. The 1D density profile of the L1498 core was taken from Tafalla et al. (2004, see their Table 2) and is

$$n(r) = \frac{0.94 \times 10^5}{1 + (r(''){/}75'')^{3.5}} \text{ cm}^{-3}. \quad (1)$$

For the temperature radial profile, we have used the T_{kin} values derived by Tafalla et al. (2004) from NH$_3$ observations for L1498 (see their Section 3.1 and Figure 4) and assumed a temperature radial distribution similar to the one employed by Chacón-Tanarro et al. (2019) for the L1544 prestellar core. We also assume that the gas and dust temperatures are equal. The temperature profile is fitted as

$$T(r) = 13.0 - \frac{13.0 - 10.0}{1.0 + (r('')/90'')^{1.7}} \text{ K}. \quad (2)$$

The radial distribution of the H$_2$ volume gas density and the temperature assumed for the L1498 starless core are shown in Figure 5 (see also Tafalla et al. 2004). For comparison, in this figure we have also included the physical structure derived by Chacón-Tanarro et al. (2019) for the L1544 prestellar core. From Figure 5, it is clear that the physical structure of both cores is different: L1498 shows a flatter gas density profile and lower peak H$_2$ gas density with respect to L1544, and its temperature at the center never gets below 10 K as observed in L1544.

Using the physical structure of L1498, the chemical evolution of the core is then calculated toward 150 radial points with 1″ spatial spacing. To simulate the chemical evolution at every radial point, we utilized the 0D gas-grain chemical model MONACO. This is a rate-equations-based, three-phase (gas/ice surface/ice bulk) numerical model that provides the evolution of the fractional abundances of atomic and molecular species with time. The model is based on the work by Vasyunin & Herbst (2013) and was successfully applied to reproduce the abundances of O-bearing COMs in the prototypical L1544 prestellar core (Vasyunin et al. 2017). In this model, the precursors of both O-bearing and N-bearing COMs are formed on the surface of dust grains via hydrogenation. Once formed, a small fraction of these

precursors is nonthermally desorbed from dust grains (see details below on the nonthermal processes assumed) and undergoes subsequent gas-phase reactions that produce the observed COMs (see Vasyunin & Herbst 2013; Vasyunin et al. 2017).

Before this study, minor updates had been introduced in the chemical network of the MONACO code as described in Lattanzi et al. (2020; see the reactions described in their Table 2). However, in our work, we have found an enhanced set of N-bearing species, which includes species such as CH$_2$CHCN, HCCNC, and CH$_3$NC. Thus, we have further expanded our chemical network to account properly for the chemistry of those species. In particular, we have expanded the gas and grain chemistry of hydrocarbons (C$_x$H$_y$) following Hickson et al. (2016). This has enabled us to add the formation route of CH$_2$CHCN via the gas-phase reactions N + C$_3$H$_5$ → CH$_2$CHCN + H$_2$ presented in the KIDA database to the gas-phase and grain-surface routes already present in our network, namely the surface hydrogenation of HC$_3$N and the gas-phase reaction CN + C$_2$H$_4$ → CH$_2$CHCN + H. We note, however, that the reaction between N and C$_3$H$_5$ has not been studied in detail, and it may not lead to CH$_2$CHCN as a product (J. C. Loison 2020, private communication). The chemical networks of HCCNC and CH$_3$NC were added following the approach described in Vastel et al. (2019) and Willis et al. (2020).

It has been shown before that interstellar chemistry is an interplay between gas-phase and grain-surface chemical processes connected via the processes of accretion and desorption, and with surface chemistry being especially important for the formation of COMs (see, e.g., Herbst & van Dishoeck 2009; Agúndez & Wakelam 2013). At the low temperatures of 10 K typical of prestellar cores, desorption of species from dust grains to the gas phase requires additional energy, which is the result of either exothermic surface reactions or the interaction of icy grain mantles with energetic particles such as cosmic rays or photons produced by cosmic rays. Although the details are still known poorly, many observational results such as widespread presence of methanol in cold gas imply nonzero efficiency of desorption from grains even at 10 K.

In our model, in addition to thermal evaporation, photodesorption, cosmic-ray-induced desorption (Hasegawa & Herbst 1993), and reactive (chemical) desorption (Minissale et al. 2016) are included. While cosmic-ray-induced desorption is known to have limited effects on the abundances of COMs, the case of reactive desorption is more complicated. Several theoretical and experimental studies of reactive desorption arrive at somewhat different conclusions on reactive desorption efficiency for various chemically reacting systems (see Garrod et al. 2007; Minissale et al. 2016; Chuang et al. 2018; Fredon & Cuppen 2018). The point of consensus is probably that the COMs with a large number of atoms (>6) do not desorb from grains via the mechanism of reactive desorption because the energy released during the exothermic surface reaction event likely gets redistributed and relaxed between the numerous internal degrees of freedom of a product molecule rather than breaking the bond between the product molecule and the surface. In this study, we use the parameterization of the efficiency of reactive desorption proposed in Minissale et al. (2016), the same as in Vasyunin et al. (2017). Note that a natural outcome of this parameterization is that the efficiency of chemical reactive desorption for large COMs (with more than 6 atoms such as e.g., CH$_2$CHCN) is negligible (see below).

Other assumptions made for the surface chemistry are also the same as in Vasyunin et al. (2017): the tunneling for surface
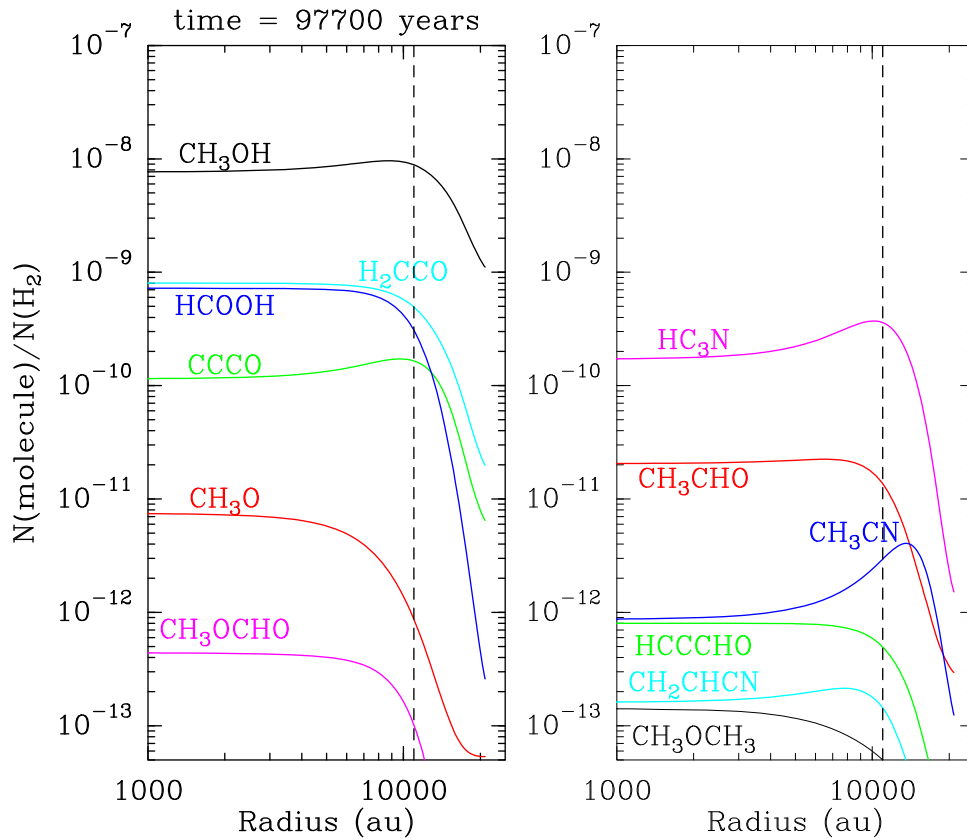
Figure 6. Radial distributions of modeled fractional abundances of species considered in this study. Fractional abundances are derived as column density ratios convolved with a 26″ beam. A radius $r = 0$ au corresponds to the location of the dust peak. Vertical dashed lines indicate the radius associated with the location of the methanol peak in L1498.

diffusion of H and H_2 is enabled, and the diffusion-to-binding energy ratio $E_{diff}/E_{bind} = 0.3$. The initial abundances of the species considered in the modeling were obtained from the final abundances of the simulation of a diffuse cloud model with $A_V = 2$ mag, gas and dust temperatures of 20 K, and gas density of 10^2 cm^{-3} over 10^7 yr using the "low metals" initial abundances EA1 from Wakelam & Herbst (2008).

Using the physical and chemical setup described above, we performed the chemical modeling of the L1498 starless core over a time span of 10^6 yr and compared the modeling results with our observations. We found that the best fit between the observed and the predicted fractional abundances of the O-bearing and N-bearing COMs (calculated using the modeled column densities convoluted with the 26″ IRAM 30 m beam) is reached at an age of 9×10^4 yr for the L1498 starless core. The best-fit COMs abundances are presented in Table 5, where we consider that the observed and predicted abundances are in agreement if both differ by less than a factor of 10.

In Figure 6, we report the results of the abundance distribution of O-bearing and N-bearing COMs as a function of radius obtained for the L1498 starless core for our best-fit model. Interestingly, the predicted COMs abundances show a maximum in their distribution at a radial distance between 10,000 au and 14,000 au, which is consistent with the observed behavior (Tafalla et al. 2006). Note that this distance is three times farther away than found toward L1544 ($\sim$4000 au in L1544; see Vasyunin et al. 2017) and it is a consequence of the flatter density distribution of the L1498 starless core. Our model also reproduces the lack of detections of O-bearing COMs such as CH_3OCHO and CH_3OCH_3 in L1498 as opposed

to L1544. Indeed, the predicted abundances of these molecules for our L1498 model fall well below the value of 1×10^{-12}, which is consistent with the measured upper limits for these species toward this core (see Table 3 and Section 3).

Note, however, that the COM and COM precursor abundance enhancement predicted by the model at distances $\sim$11,000 au is less pronounced than that predicted by the same model for L1544. This is probably due to the fact that the H_2 gas density toward L1498's dust peak is moderate ($\sim$10^5 cm^{-3}, i.e., two orders of magnitude lower than that measured for L1544) and thus, it does not induce such a strong molecular depletion in the L1498's model compared to L1544's one. The angular resolution of the MAMBO 1.2 mm map of L1498 is however $\sim$11″ and, as in the case of L183 (Lattanzi et al. 2020), we cannot rule out the possibility that within the innermost $\leqslant$2000 au of L1498, the actual H_2 gas density is higher than $\sim$10^5 cm^{-3}, as derived by Tafalla et al. (2004).

Despite this caveat, Table 5 shows that our model matches (overall) the abundances of most O-bearing and N-bearing COMs and COM precursors measured toward L1498, with the exception of CH_3OH and CH_2CHCN.[10] For CH_3OH, our model overproduces this molecular species in the gas phase toward L1498's dust peak by a factor of $\sim$40, while it predicts an abundance within a factor of $\sim$7 for the position of the methanol peak. Note that this overproduction was already noted by Punanova et al. (2018) for the case of L1544, although in the case of L1498 it is more likely related to a

---

[10] H_2CCO shows a disagreement by a factor of just $\sim$10 toward the position of L1498's methanol peak (Table 5).

milder depletion of the molecular gas toward the innermost regions of the core (see above).

For CH_2CHCN, this molecule is firmly detected toward both positions in the L1498 starless core with abundances of $(1.3–1.6) \times 10^{-10}$ (Table 5), while the modeled values are up to three orders of magnitude lower. The low abundance of CH_2CHCN is maintained not only at the moment of the best agreement between the model and observations but over the whole time span of the simulation: it never exceeds a few $\times 10^{-12}$. This means that the proposed gas-phase formation routes of CH_2CHCN (i.e., $N + C_3H_5 \rightarrow CH_2CHCN + H_2$ and $CN + C_2H_4 \rightarrow CH_2CHCN + H$; see above) are not sufficient to produce the observed amount of this species in the L1498 starless core. Alternatively, on grain surfaces, CH_2CHCN forms mainly via the hydrogenation of HC_3N. However, this grain-surface formation does not contribute significantly to the gas-phase abundance of CH_2CHCN due to the near-zero efficiency of reactive desorption of this species from the grains (of $\sim 10^{-6}$, as calculated following the formalism of Minissale et al. 2016). This is in agreement with Garrod et al. (2017), who also arrived at the conclusion that the modeled gas-phase abundance of CH_2CHCN does not exceed 10^{-11} at low temperatures.

To reproduce the abundances of CH_2CHCN measured toward L1498, we have tested arbitrary values for the efficiency of reactive desorption of this species. An efficiency of 1% is sufficient to reproduce the observed gas-phase abundance of 1.5×10^{-10} for CH_2CHCN simultaneously with the rest of the species. This implies that either chemical reactive desorption is somehow efficient for this molecule in particular or that there is an additional mechanism responsible for the desorption of these large COMs besides chemical reactive desorption. The direct impact of cosmic rays on dust grains has been proposed to be a factor of 10 more efficient than chemical reactive desorption (see Dartois et al. 2019, 2020), which could increase the desorption efficiency of large COMs from grains. Note, however, that if this were the case, CH_2CHCN would have to survive on the grain surface over the period between its formation and independent desorption, which in our current model is unlikely because this molecule is further hydrogenated into ethyl cyanide (C_2H_5CN) on the grain surface. Further experimental and theoretical work on the grain chemistry and desorption mechanisms of N-bearing COMs such as C_2H_5CN at low temperatures is needed.

We finally note that the best-fit chemical age derived for L1498 is shorter than that for L1544 (9×10^4 yr versus 1.6×10^5 yr; Vasyunin et al. 2017). L1498 indeed shows a flatter density profile distribution than L1544, and its deuterium fractionation is consistent with the core being at an earlier evolutionary stage (Tafalla et al. 2004; Crapsi et al. 2005). The younger chemical age of L1498 is also supported by the smaller abundance difference found for methanol between its dust and methanol peaks, with respect to that measured toward L1544 (see Figure 4). This can be explained by the smaller degree of CO freeze-out in L1498, which in turn indicates a less evolved core for L1498 as compared to L1544. A shorter age would also explain why L1498 is accreting material from the molecular cloud onto the core but does not show any infall signatures within the core itself yet (Tafalla et al. 2004).

6. Conclusions

As shown in Section 3, our high-sensitivity observations carried out toward the L1498 starless core reveal that O-bearing COMs such as CH_3CHO, CH_3OCHO, and CH_3OCH_3 are detected neither toward the dust peak nor toward the outer regions of the core where CH_3OH peaks (i.e., at $\sim 10,000$ au from the core's center). This behavior is in contrast with the one observed toward the L1544 prestellar core, where these large O-bearing COMs not only are detected toward this outer region, but their abundances present their maximum values at a distance of only ~ 4000 au with respect to the center of the L1544 core.

For N-bearing COMs, these species are systematically enhanced toward the outer regions of the L1498 starless core, in agreement with what was previously found toward L1544, and even in higher amounts. The distance at which the enhancement of the N-bearing COMs occurs in L1498 is, however, much larger than that found in L1544 ($\sim 10,000$ au versus ~ 4000 au).

We have investigated the origin of the differences observed in the behavior of COMs between L1498 and L1544 by carrying out chemical modeling of both O-bearing and N-bearing COMs using the known physical structure of the L1498 starless core (Section 5). Our modeling results reveal that the enhancement of N-bearing COMs in the outer shells of L1498 at distances of $\sim 10,000$ au, is the expected outcome of the interplay between the gas phase and the surface of dust grains given the flatter density radial profile of L1498 in comparison to the more evolved prestellar core L1544. Therefore, the different content in O-bearing and N-bearing complex organic material in starless and prestellar cores is a consequence not only of their physical structure but also of their evolution.

Facility: IRAM 30 m telescope.

Software: MADCUBA (Martín et al. 2019), MONACO (Vasyunin et al. 2017).

ORCID iDs

Izaskun Jiménez-Serra ⦿ https://orcid.org/0000-0003-4493-8714
Anton I. Vasyunin ⦿ https://orcid.org/0000-0003-1684-3355
Paola Caselli ⦿ https://orcid.org/0000-0003-1481-7911
Giuliana Cosentino ⦿ https://orcid.org/0000-0001-5551-9502
Serena Viti ⦿ https://orcid.org/0000-0001-8504-8844

References

Agúndez, M., Marcelino, N., Cernicharo, J., Roueff, E., & Tafalla, M. 2019, A&A, 625, A147
Agúndez, M., & Wakelam, V. 2013, ChRv, 113, 8710
Bacmann, A., Taquet, V., Faure, A., Kahane, C., & Ceccarelli, C. 2012, A&A, 541, L12
Balucani, N., Ceccarelli, C., & Taquet, V. 2015, MNRAS, 449, L16
Belloche, A., Menten, K. M., Comito, C., et al. 2008, A&A, 482, 179
Belloche, A., Müller, H., Menten, K., Schilke, P., & Comito, C. 2013, A&A, 559, A47
Bizzocchi, L., Caselli, P., Spezzano, S., & Leonardo, E. 2014, A&A, 569, A27
Bohlin, R. C., Savage, B. D., & Drake, J. F. 1978, ApJ, 224, 132
Bottinelli, S., Ceccarelli, C., Lefloch, B., et al. 2004, ApJ, 615, 354
Caselli, P., Walmsley, C. M., Zucconi, A., et al. 2002, ApJ, 565, 331
Cernicharo, J., Marcelino, N., Roueff, E., et al. 2012, ApJL, 759, L43
Chacón-Tanarro, A., Pineda, J. E., Caselli, P., et al. 2019, A&A, 623, A118
Charnley, S. B., Kress, M. E., Tielens, A. G. G. M., & Millar, T. J. 1995, ApJ, 448, 232
Chuang, K.-J., Fedoseev, G., Qasim, D., et al. 2018, ApJ, 853, 102
Chuang, K.-J., Fedoseev, G., Ioppolo, S., van Dishoeck, E. F., & Linnartz, H. 2016, MNRAS, 455, 1702
Crapsi, A., Caselli, P., Walmsley, C. M., et al. 2005, ApJ, 619, 379
Dartois, E., Chabot, M., Bacmann, A., et al. 2020, A&A, 634, A103
Dartois, E., Chabot, M., Id Barkach, T., et al. 2019, A&A, 627, A55
Endres, C. P., Schlemmer, S., Schilke, P., Stutzki, J., & Müller, H. S. P. 2016, JMoSp, 327, 95
Fedoseev, G., Sciré, C., Baratta, G. A., & Palumbo, M. E. 2018, MNRAS, 475, 1819
Fredon, A., & Cuppen, H. M. 2018, PCCP, 20, 5569
Friberg, P., Hjalmarson, A., Madden, S. C., & Irvine, W. M. 1988, A&A, 195, 281
Galli, P. A. B., Loinard, L., Bouy, H., et al. 2019, A&A, 630, A137
Garrod, R. T., Belloche, A., Müller, H. S. P., & Menten, K. M. 2017, A&A, 601, A48
Garrod, R. T., Weaver, S. L. W., & Herbst, E. 2008, ApJ, 682, 283
Garrod, R. T., Wakelam, V., & Herbst, E. 2007, A&A, 467, 1103
Harju, J., Pineda, J. E., Vasyunin, A. I., et al. 2020, ApJ, 895, 101
Hasegawa, T. I., & Herbst, E. 1993, MNRAS, 263, 589
Herbst, E., & van Dishoeck, E. F. 2009, ARA&A, 47, 427
Hickson, K. M., Wakelam, V., & Loison, J.-C. 2016, MolAs, 3, 1
Holdship, J., Viti, S., Codella, C., et al. 2019, ApJ, 880, 138
Hollis, J. M., Lovas, F. J., Remijan, A. J., et al. 2006, ApJL, 643, L25
Hollis, J. M., Lovas, F. J., & Jewell, P. R. 2000, ApJL, 540, L107
Ivlev, A. V., Röcker, T. B., Vasyunin, A., & Caselli, P. 2015, ApJ, 805, 59
Jiménez-Serra, I., Vasyunin, A. I., Caselli, P., et al. 2016, ApJL, 830, L6
Jin, M., & Garrod, R. T. 2020, ApJS, 249, 26
Jorgensen, J. K., Favre, C., Bisschop, S. E., et al. 2012, ApJL, 757, L4
Lattanzi, V., Bizzocchi, L., Vasyunin, A. I., et al. 2020, A&A, 633, A118
Marcelino, N., Cernicharo, J., Agúndez, M., et al. 2007, ApJ, 665, L127
Martín, S., Martín-Pintado, J., Blanco-Sánchez, C., et al. 2019, A&A, 631, A159
Minissale, M., Moudens, A., Baouche, S., Chaabouni, H., & Dulieu, F. 2016, MNRAS, 458, 2953
Öberg, K. I., Bottinelli, S., Jorgensen, J. K., & van Dishoeck, E. F. 2010, ApJ, 716, 825
Pickett, H. M., Poynter, R. L., Cohen, E. A., et al. 1998, JQSRT, 60, 883
Punanova, A., Caselli, P., Feng, S., et al. 2018, ApJ, 855, 112
Quénard, D., Jiménez-Serra, I., Viti, S., Holdship, J., & Coutens, A. 2018, MNRAS, 474, 2796
Redaelli, E., Bizzocchi, L., Caselli, P., et al. 2019, A&A, 629, A15
Rawlings, J. M. C., Williams, D. A., Viti, S., & Cecchi-Pestellini, C. 2013, MNRAS, 430, 264
Ruaud, M., Loison, J. C., Hickson, K. M., et al. 2015, MNRAS, 447, 4004
Scibelli, S., & Shirley, Y. 2020, ApJ, 891, 73
Shingledecker, C. N., Tennis, J., Le Gal, R., & Herbst, E. 2018, ApJ, 861, 20
Soma, T., Sakai, N., Watanabe, Y., & Yamamoto, S. 2018, ApJ, 854, 116
Spezzano, S., Caselli, P., Bizzocchi, L., Giuliano, B. M., & Lattanzi, V. 2017, A&A, 606, A82
Spezzano, S., Bizzocchi, L., Caselli, P., Harju, J., & Brünken, S. 2016, A&A, 592, L11
Tafalla, M., Myers, P. C., Caselli, P., & Walmsley, C. M. 2004, Ap&SS, 292, 347
Tafalla, M., Santiago-García, J., Myers, P. C., et al. 2006, A&A, 455, 577
Van der Tak, F. F. S., Black, J. H., Schöier, F. L., Jansen, D. J., & van Dishoeck, E. F. 2007, A&A, 468, 627
Vastel, C., Loison, J. C., Wakelam, V., & Lefloch, B. 2019, A&A, 625, A91
Vastel, C., Ceccarelli, C., Lefloch, B., & Bachiller, R. 2014, ApJL, 795, L2
Vasyunin, A. I., Caselli, P., Dulieu, F., & Jiménez-Serra, I. 2017, ApJ, 842, 33
Vasyunin, A. I., & Herbst, E. 2013, ApJ, 769, 34
Wakelam, V., & Herbst, E. 2008, ApJ, 680, 371
Watanabe, N., & Kouchi, A. 2002, ApJL, 571, L173
Willis, E. R., Garrod, R. T., Belloche, A., et al. 2020, A&A, 636, A29
Wirström, E. S., Geppert, W. D., Hjalmarson, Å, et al. 2011, A&A, 533, A24
Yoshida, K., Sakai, N., Nishimura, Y., et al. 2019, PASJ, 71, 18